RL-TR-93-225
Final Technical Report
November 1993

MODELING, ANALYSIS, AND SIMULATION OF AN OPTICAL TIME-DIVISION MULTIPLE-ACCESS NETWORK ARCHITECTURE

North Carolina State University

Michael Devetsikiotis, Quing G. Zhou, Gavin R. Cato,
J. Keith Townsend, and Robert M. Kolbas

APPROVED FOR PUBLIC RELEASE; DISTRIBUTION UNLIMITED.

Rome Laboratory
Air Force Materiel Command
Griffiss Air Force Base, New York

This report has been reviewed by the Rome Laboratory Public Affairs Office (PA) and is releasable to the National Technical Information Service (NTIS). At NTIS it will be releasable to the general public, including foreign nations.

RL-TR-93-225 has been reviewed and is approved for publication.

APPROVED: Raymond K. Boncek

RAYMOND K. BONCEK
Project Engineer

FOR THE COMMANDER: Luke L Lucas

LUKE L. LUCAS, Colonel, USAF
Deputy Director
Surveillance & Photonics Directorate

If your address has changed or if you wish to be removed from the Rome Laboratory mailing list, or if the addressee is no longer employed by your organization, please notify RL (OCPA) Griffiss AFB NY 13441. This will assist us in maintaining a current mailing list.

Do not return copies of this report unless contractual obligations or notices on a specific document require that it be returned.

REPORT DOCUMENTATION PAGE

Form Approved
OMB No. 0704-0188

1. AGENCY USE ONLY (Leave Blank)	2. REPORT DATE	3. REPORT TYPE AND DATES COVERED
	November 1993	Final Mar 92 - Sep 93

4. TITLE AND SUBTITLE
MODELING, ANALYSIS, AND SIMULATION OF AN OPTICAL TIME-DIVISION MULTIPLE-ACCESS NETWORK ARCHITECTURE

5. FUNDING NUMBERS
C - F30602-92-C-0016
PE - 62702F
PR - 4600
TA - P2
WU - PH

6. AUTHOR(S)
Michael Devetsikiotis, Qing G. Zhou, Gavin R. Cato, J. Keith Townsend, and Robert M. Kolbas

7. PERFORMING ORGANIZATION NAME(S) AND ADDRESS(ES)
North Carolina State University
Dept of Electrical & Computer Engineering
Raleigh NC 27695

8. PERFORMING ORGANIZATION REPORT NUMBER
N/A

9. SPONSORING/MONITORING AGENCY NAME(S) AND ADDRESS(ES)
Rome Laboratory (OCPA)
25 Electronic Pky
Griffiss AFB NY 13441-4515

10. SPONSORING/MONITORING AGENCY REPORT NUMBER
RL-TR-93-225

11. SUPPLEMENTARY NOTES
Rome Laboratory Project Engineer: Raymond K. Boncek/OCPA/(315) 330-2937

12a. DISTRIBUTION/AVAILABILITY STATEMENT
Approved for public release; distribution unlimited.

12b. DISTRIBUTION CODE

13. ABSTRACT (Maximum 200 words)

An optical time-division multiple-access (OTDMA) network architecture has been proposed which has the potential of avoiding electronic processing of signals at the aggregate network bandwidth. New specifications for the optical components used in this OTDMA network architecture will be required before a practical system is realized. In this report, we present a model of the OTDMA architecture that relates parameters at the device level such as carrier mobility, physical geometry, charge trapping, and carrier-concentration to system-level performance measures such as bit error rate and noise margin. We present mathematical models of the devices in the system. These models are interconnected into a system-level Monte Carlo simulation model of the OTDMA architecture.

14. SUBJECT TERMS	15. NUMBER OF PAGES
Monte Carlo Device Simulation, Time-Division Multiple-Access, Optical Network, Optical Interconnect, Device Modeling, Neural Networks, Optical Correlator, Optical AND Gate	56
	16. PRICE CODE

17. SECURITY CLASSIFICATION OF REPORT	18. SECURITY CLASSIFICATION OF THIS PAGE	19. SECURITY CLASSIFICATION OF ABSTRACT	20. LIMITATION OF ABSTRACT
UNCLASSIFIED	UNCLASSIFIED	UNCLASSIFIED	UL

Contents

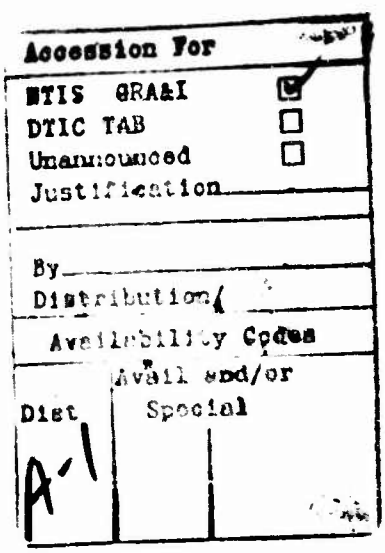

Modeling, Analysis, and Simulation of an Optical Time-Division Multiple-Access Network Architecture

Michael Devetsikiotis, Qing G. Zhou, Gavin R. Cato, J. Keith Townsend, Robert M. Kolbas
Center for Communications and Signal Processing and
The Department of Electrical & Computer Engineering,
North Carolina State University, Raleigh, NC 27695

Raymond Boncek, Mark Krol, John Stacy
Rome Laboratory Photonics Center,
Griffis AFB, NY 13441

Abstract

An optical time-division multiple-access (OTDMA) network architecture has been proposed which has the potential of avoiding electronic processing of signals at the aggregate network bandwidth. New specifications for the optical components used in this OTDMA network architecture will be required before a practical system is realized.

In this report, we present a model of the OTDMA architecture that relates parameters at the device level such as carrier mobility, physical geometry, charge trapping, and carrier-concentration to system-level performance measures such as bit error rate and noise margin. We present mathematical models of the devices in the system. These models are interconnected into a system-level Monte Carlo simulation model of the OTDMA architecture.

The photoconductive AND device, a critical component in the OTDMA receiver, is modeled as a time-varying circuit element (conductance) in a microstrip transmission line. Device-level physics of the photoconductor is incorporated into the microstrip model via a time-varying conductance.

We base the simulation model of the AND device on the explicit second order Adams-Bashforth formulation. Alternative simulation modeling approaches, including feed-forward artificial neural networks, are also used with excellent results. Simulation of the OTDMA network is in good agreement with our approximate analysis, in addition to laboratory measurements.

1 Introduction

The large potential bandwidth of optical fiber — theoretically on the order of 20×10^{12} Hz — cannot be realized by simply replacing the existing communications medium with optical fiber. To fully utilize the potential bandwidth of optical fiber in multiple-access applications such as local area communication networks and high speed computer interconnects, the large aggregate bandwidth of the network must be processed optically. This avoids the "electronic bottleneck" imposed if the network is implemented electronically. The bottleneck results because the network must process data at the rate $N \times B_E$, where N is the number of users and B_E is the bandwidth limit for electronic processors. Thus, the data rate of each node in the network must be reduced by a factor of N for an electronic network implementation.

One approach which has the potential to achieve this objective is based on time-division multiple-access [1]. Critical devices to implement such an optical time-division multiple-access (OTDMA) network include a high contrast ratio photoconductive AND device, a rapidly tunable optical delay device, and high bandwidth electro-optic modulators. Recently, a rapidly tunable OTDMA coder was demonstrated at the Rome Laboratory Photonics Center [2]. Good performance for 64 100 Mb/s channels was observed. A 5 Gb/s 50 channel OTDMA network has also been demonstrated in the [3], although this implementation is ultimately limited by the bandwidth of the pre-amplifier.

In this demonstration, a photoconductive AND device with a contrast ratio of 2 was used, thus requiring high bandwidth electronic processing at the detection filter in the receiver -- imposing a potential electronic bottleneck, but still providing large throughput.

Higher contrast ratio configurations using photoconductive AND devices have been reported [4, 5]. However, these high contrast ratios were achieved by the use of electronic devices operating at the aggregate network bandwidth. We show in the sequel that a low contrast ratio significantly impairs system performance.

Other degradations which affect performance of the network at the *system* level include crosstalk from adjacent channels, timing jitter due to noise and crosstalk, timing offset due to small length variations of the fiber, interference caused by crosstalk in the tunable coder switches, relative intensity noise in the laser, and thermal and shot noise in the receiver. These impairments all increase the bit error rate (BER) of the system.

In general, the BER of the system is a function of the physical devices used in the system as well as the system architecture. The relationship between device level parameters and system level performance (such as BER) is typically not straightforward, and is thus not analytically tractable. Many times in these cases, simulation is a viable alternative.

In this report, we present a model of the OTDMA network architecture that relates parameters at the device-level such as carrier mobility, physical geometry, charge trapping, and carrier-concentration to system-level performance measures such as bit error rate and noise margin. The effect of other degradations such as timing errors and detection filter bandwidth, as well as device parameter values on system performance are also studied. This is accomplished by developing mathematical models of the optical and electronic devices in the system which are suitable for discrete-time Monte Carlo simulation at the system-level.

These simulation models are interconnected into a system level simulation model of the OTDMA architecture. We demonstrate some of the capabilities of the simulation model through a number of examples at both the device and system-level. In this report we focus on the photoconductive AND device, since its performance is critical to the OTDMA network. Both analytical and simulation-based analysis of the effects of non-infinite contrast ratio on BER performance of the system are presented. Using simulation, we also determine the system noise margin — a measure of the system's immunity to noise — as a function of the detection filter bandwidth and timing error.

Usually the description of devices used in communication systems involves solving a set of simultaneous, nonlinear, partial differential equations. Unless some simplifications can be made, such detailed models are often too time consuming to be useful in a *system-level* simulation where the nonlinear device is just one of many subsystems. Therefore,

higher-level models are needed that approximate the input-output behavior, without necessarily resorting to the fundamental physics of the device [6].

The literature on the characterization of nonlinear functionals includes the work of Volterra, Wiener and others. Using the Stone-Weierstrass theorem it can be shown that a given nonlinear functional under certain conditions can be represented by a corresponding series such as the Volterra series or the Wiener series [7, 8, 9]. Despite their theoretical importance and the insights they offer, such representations have not received wide application in the identification of large classes of practical nonlinear systems.

Because of the importance the photoconductive AND device has on overall OTDMA system performance, we investigate simulating devices and subsystems that are originally described by nonlinear differential equations (NLDE). Such nonlinear models are widely used in the systems and the control literature, usually in the form of state-space representations and state equations.

Models based on directly solving detailed differential equations can be too time consuming to be useful in a system simulation where the nonlinear device is just one of many subsystems. For simulation applications nonlinearities are more efficiently represented as a functional relationship or in tabular form. Due to the computational burden, the increased complexity, and the stability problems imposed by directly simulating the NLDE, it is often desirable to compute and implement non-NLDE based models [6].

One family of such models are those based on the Volterra or the Wiener series [7, 8]. As mentioned in [9], such approaches suffer from the rapid explosion of the possible combination of terms as the order of the polynomial increases. In the multivariable case, beside the increased complexity of the formulation one also has to cope with the dramatically increasing computational burden in training as well as in on-line simulation run time required by such models.

Explicit input-output, block simulation models for nonlinearities have been proposed for specific cases of communications devices and subsystems [6]. However, there still is a need for a more general, robust methodology for modeling nonlinear subsystems, especially for the purpose of efficient simulation. Here we investigate an alternative

modeling and simulation paradigm that involves *artificial neural networks* (ANN). We use this ANN technique to model the photoconductive AND device, and compare its accuracy and efficiency to the NLDE-based model.

Our goal is to propose a way to exploit the large available amount of neural network architectures and learning methods in order to improve the simulation efficiency of communication systems involving nonlinearities. Whereas recent work has focused on the use of ANN for the identification and control of dynamical systems ([10, 11] and references within), we focus on using ANN to identify nonlinear systems for simulation purposes. The growing wealth of neural net structures and techniques presents an appealing family of modeling tools not only to the control but also to the simulation practitioner.

Our comparison in Section 4.3 indicates that ANN-based block models can be preferable to direct differential equation-based models in terms of generality, robustness and run time efficiency. At the price of some initial overhead for training, such block models can be advantageous especially for simulation studies involving repetitions of lengthy runs at the system level. Furthermore, in cases where training data can be obtained without formulating a NLDE model, the ANN-based approach has additional advantages since it eliminates the time and effort required to formulate the NLDE model. In some cases, the last argument could be the dominant reason for using ANN.

The experimental results obtained from using feed-forward ANN to simulate a two input optoelectronic AND device are in good agreement with the corresponding differential equation model, and indicate significant run time savings over the linear multistep integration method, both at the device- and at the system-simulation-level.

An interesting conclusion from this work is that to reduce the I&D filter bandwidth in the receiver to the bandwidth of an individual electronic processor, the contrast ratio of the photoconductive AND device must be much larger than 2:1 for a large network. Also, for the device studied in this report, at Gb/s speeds, device geometry has a much stronger influence on the contrast ratio than other device parameters.

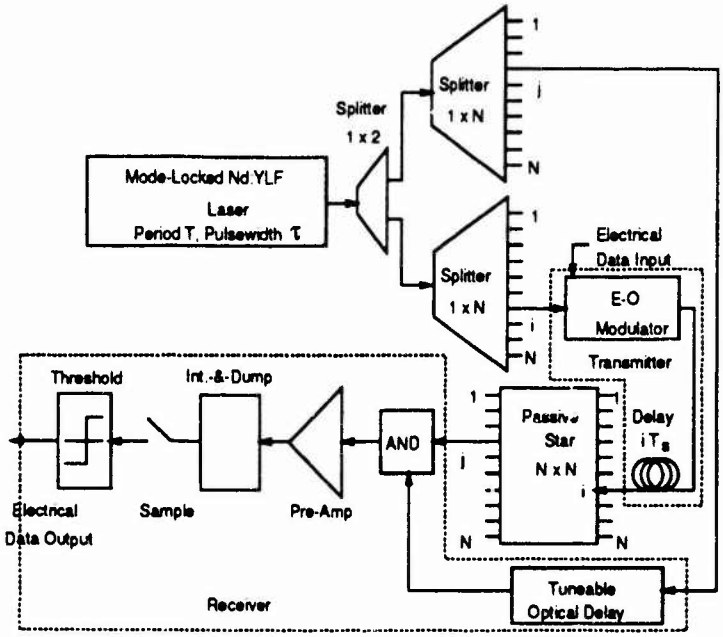

Figure 1: Block diagram of the OTDMA system. The i^{th} transmitter and j^{th} receiver are shown.

2 System Description

A block diagram of the OTDMA network discussed in this report is shown in Fig. 1. Narrow pulses of width τ and repetition period T, where $T = NT_s$, T_s is the slot width, and N is the number of users, are generated in this system by a mode-locked Nd:YLF laser. Thus, the laser generates one pulse per frame. The pulses are distributed to each transmitter and receiver via a $1 \times N$ splitter. A fixed-transmitter system is shown, where each transmitter has a unique address, determined by the time delay of the transmitter output signal. A receiver selects the desired transmitter by appropriately adjusting the delay of the incoming clock pulse. A self-clocked architecture has been proposed [12] which avoids the need for a separate fiber for the clock pulses, but achieves this at the expense of increased receiver complexity.

Each transmitter input is an electrical binary data stream, operating at the frame rate, which modulates the optical clock signal. The modulated optical pulse is then given a unique delay corresponding to the transmitter's address. A passive star distributes the

signal from the N transmitters to the N receivers. Electrical data is assumed to be binary, and ideally, the modulator output in each frame interval consists of a pulse of width τ delayed to the transmitter's slot. A transmitted "1" or "0" for a given frame interval is designated by the the presence or absence, respectively, of this pulse.

To detect the received optical signal, the receiver must perform an "AND" operation between the output of the star coupler and the delayed clock pulse to distinguish data in the desired slot from adjacent slots. The electrical signal at the AND output is then amplified, filtered, sampled, and thresholded to determine whether the transmitted bit is a 0 or 1. We assume here that the detection filter is an integrate-and-dump (I&D) filter, although the simulation model described in the sequel is more general.

When coupled with an I&D filter with bandwidth less than the aggregate network bandwidth, the finite contrast ratio can result in significant crosstalk from adjacent channels. The severity of this crosstalk depends heavily on the actual values of I&D bandwidth and the contrast ratio.

3 AND Device Modeling and Simulation

3.1 Mathematical Model

The photoconductive AND device in the OTDMA network consists of two photoconductors connected in series. There are several models to describe photoconductors [27, 28, 29, 30, 31, 32, 33, 34, 35, 36, 37, 38, 39]. A commonly used approach is to model the photoconductor as a time-varying conductance connected in parallel with a capacitance [39]. This approach neglects retardation effects, time dependent capacitances, nonlinear effects from semiconductor-metal contacts, velocity saturation, and details of the relaxation kinetics of the optically generated carriers. Since our simulation concentrates on temporal responses on the order of 10-50 picoseconds, these limitations are not a problem. The benefit of this model is that it is simple and can be easily incorporated in the network simulation. Also, as will be shown, the numerical results are consistent with experimental data obtained at Rome Laboratory Photonics Center.

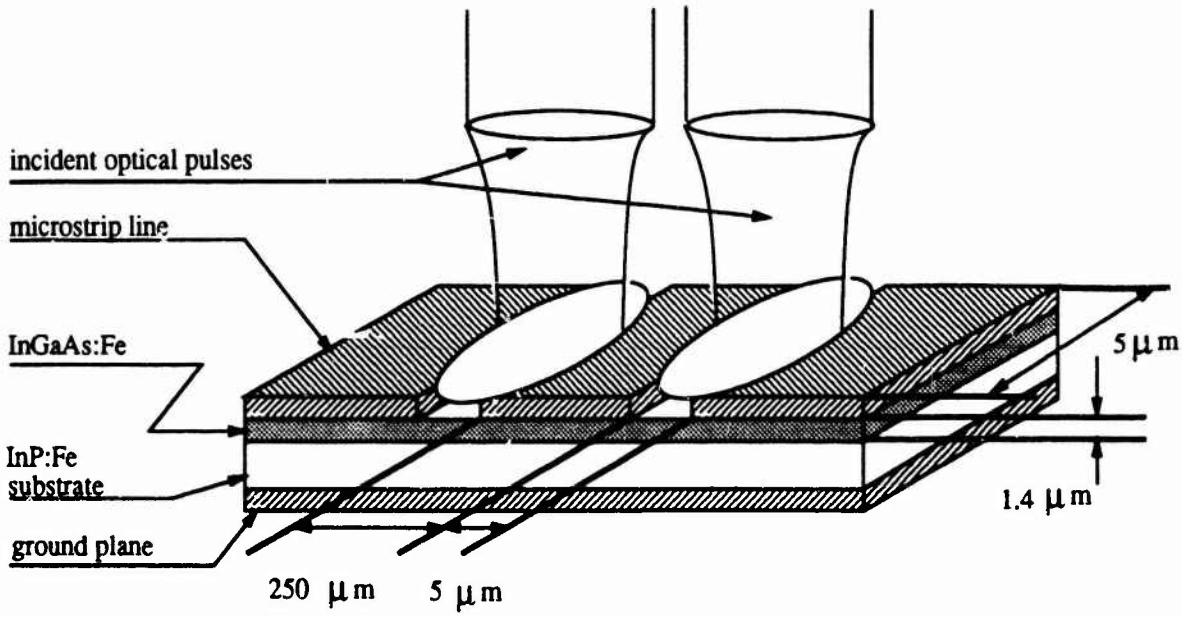

Figure 2: Schematic representation of a photoconductive AND device in a microstrip transmission line. The signal laser pulse is focused on the first gap. The clock laser pulse is applied to the second gap to sample the signal and perform the demultiplexing operation.

A schematic representation of the photoconductive AND gate is illustrated in Fig. 2. The device parameters for the low noise Fe-doped InGaAs photoconductive AND gate are as follows: electron mobility $\mu_n = 6000$ cm^2/Vs, hole mobility $\mu_p = 300$ cm^2/Vs, carrier lifetime $\tau_n = \tau_p = 20$ ps, dark resistance $1/G_0 = 10$ kΩ, and gap capacitances $C_1 = C_2 \approx 0.05$ pF. The laser pulse has a Gaussian temporal shape with a duration of 2 ps and an energy of 250 fJ which uniformly illuminates the gap. The electron trap concentration, n_t, is estimated to be 10^{15} cm^{-3}, the electron capture rate of the electron trap, C_n, is 10^{-5} s^{-1}, and the electron emission rate from the electron trap to the conductance band, E_n, is 5×10^{10} cm^3/s.

The photoconductive AND gate is represented by two series-connected photoconductors, each consisting of a time-varying conductance $G(t)$ in parallel with a capacitance C embedded in a transmission line, as indicated in Fig. 3. $V_i(t)$ is the dc bias voltage, $V_r(t)$ is the reflected wave, $V_t(t)$ is the transmitted wave, C_1 and C_2 are the capacitances

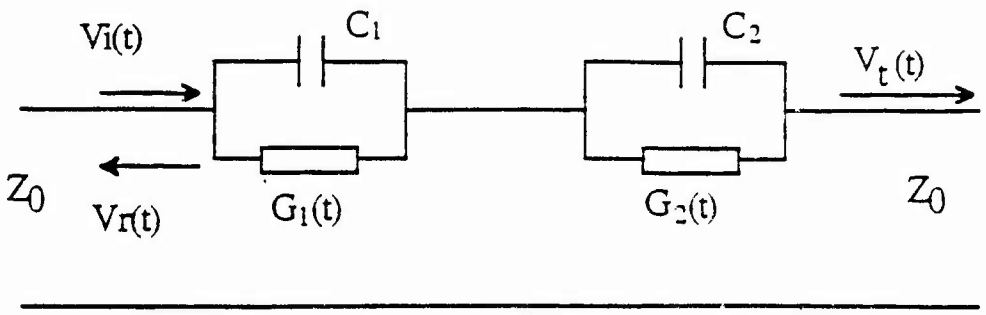

Figure 3: Lumped circuit representation of the photoconductive AND device.

of the detectors, $G_1(t)$ and $G_2(t)$ are the photoconductance of the detectors, and Z_0 is the microstrip impedance, assumed in the sequel to be $Z_0 = 50\ \Omega$.

A general expression for the conductance $G(t)$ can be derived from the rate of dissipation of electrical energy in the photoconductor and Ohm's law. By assuming a uniform carrier distribution, the conductance $G(t)$ can be represented by

$$G(t) = \frac{A}{L}(ne\mu_n + pe\mu_p) + G_0 \tag{1}$$

where n is the electron concentration, p is the hole concentration, A is the cross section area, L is length of the photoconductor, and G_0 is the dark conductance of each photodetector. The physical processes governing electrons and holes includes photogeneration, recombination, trapping and sweep-out. Since the excess carrier lifetime is less than the sweep-out time, we have neglected the sweep-out time. However we have included the effect of the trapping of carriers in deep-level impurities. The time constant for the return of the carriers from the deep levels to the bands can be quiet long, which causes a long tail in the pulse response of the device. Because the electron mobility is much greater than the hole mobility, we consider only electron trapping. The continuity equations for electrons and holes, as a function of the temporal variable t, can be written as

$$\frac{dn}{dt} = \frac{O(t)}{\hbar\omega LHW} - \frac{n}{\tau_n} - E_n n_t^- + C_n n(n_t - n_t^-) \tag{2}$$

$$\frac{dn_t^-}{dt} = E_n n_t^- - C_n n(n_t - n_t^-) \tag{3}$$

$$\frac{dp}{dt} = \frac{O(t)}{\hbar\omega LHW} - \frac{p}{\tau_p} \tag{4}$$

where $O(t)$ is the laser pulse with Gaussian shape, n_t^- is the negatively charged electron trap concentration, $\hbar\omega$ is the photon energy, τ_n and τ_p are lifetimes of the excess carriers, H is the thickness of the photoconductive film, W is the width of photoconductive film, n_t is the electron trap concentration, C_n is the electron capture rate, and E_n is the electron emission rate. Considering the effective load Z_0 of the transmission line and the traveling-wave nature of the electrical signals, the response of the device can be described in term of incident, reflected, and transmitted waves, as illustrated in Fig. 3. Since the distance between the two gaps is very small compared to the wavelength, the reflections between the two gaps can be neglected. Starting with the approach used by Auston [39], but neglecting reflections between the two gaps, the equations relating the capacitive charge $Q(t)$ and transmitted wave $V_t(t)$ are found to be:

$$\frac{V_i(t)}{Z_0} = \frac{dQ_1(t)}{dt} + \frac{Q_1(t)}{2Z_0C_1} + \frac{Q_2(t)}{2Z_0C_2} + \frac{G_1(t)}{C_1}Q_1(t) \tag{5}$$

$$\frac{V_i(t)}{Z_0} = \frac{dQ_2(t)}{dt} + \frac{Q_1(t)}{2Z_0C_1} + \frac{Q_2(t)}{2Z_0C_2} + \frac{G_2(t)}{C_2}Q_2(t) \tag{6}$$

$$V_t(t) = V_i(t) - \frac{Q_1(t)}{2C_1} - \frac{Q_2(t)}{2C_2} \tag{7}$$

where $Q_1(t)$ and $Q_2(t)$ are the instantaneous charges on the gap capacitances, and C_1 and C_2 are the gap capacitances.

These equations, with initial conditions, were solved numerically by the Runge-Kutta method. The material parameters were initially selected based on experimental values and then modified slightly to match the experimental data. The only factor that required a significant modification from the initially set value was the incident power density that generates electron-hole pairs. After taking into account the physical geometry of the fiber/detector coupling, optical reflections, and the finite thickness of the photoconductive thin film, an additional factor of 0.06371 was necessary to compensate for additional losses due to cabling and cladding modes.

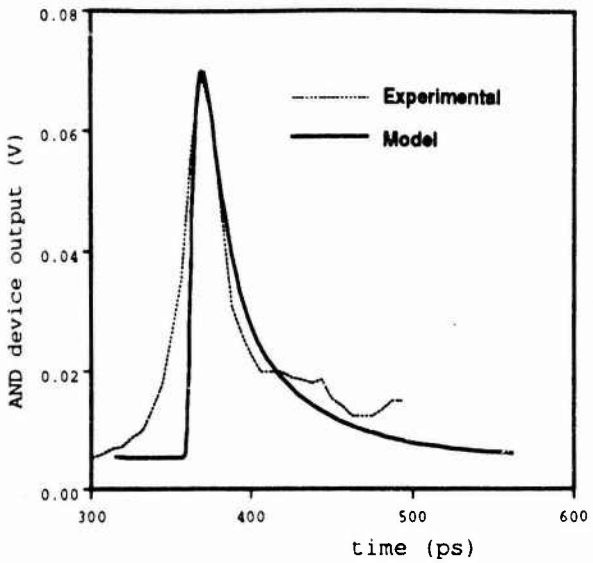

Figure 4: Temporal responses observed in the laboratory and obtained from our simulation model of the photoconductive AND device.

A comparison of the temporal responses observed in the laboratory and obtained from our simulation model for the photoconductive AND device is shown in Fig. 4. The parameter values given above were used in the simulation. The laboratory measurements were taken at the Rome Laboratory Photonics Center.

Calculated values of $V_t(t)$ versus time, for the parameter values given above, are shown in Fig. 5 (solid line). Starting at $t = 0$, the simulation relaxes to a stable state determined by the 19 KΩ dark resistance. The first pulse occurs at 200 ps when both gaps are simultaneously excited by laser pulses (1,1 state). The second and third pulses correspond to one gap illuminated while the other has no laser pulse (1,0 and 0,1 state). The dashed curve does not include trapping effects. The solid line includes trapping effects and corresponds quite well to the experimental data. Note that in both cases the contrast ratio is approximately 2:1.

Four different cases using two different laser pulse energies, 50 fJ and 500 fJ, and two different bias voltages, 0.5 V and 4 V, are plotted as shown in Fig. 6. The output voltage response increases with increasing laser energy or increasing bias voltage. The

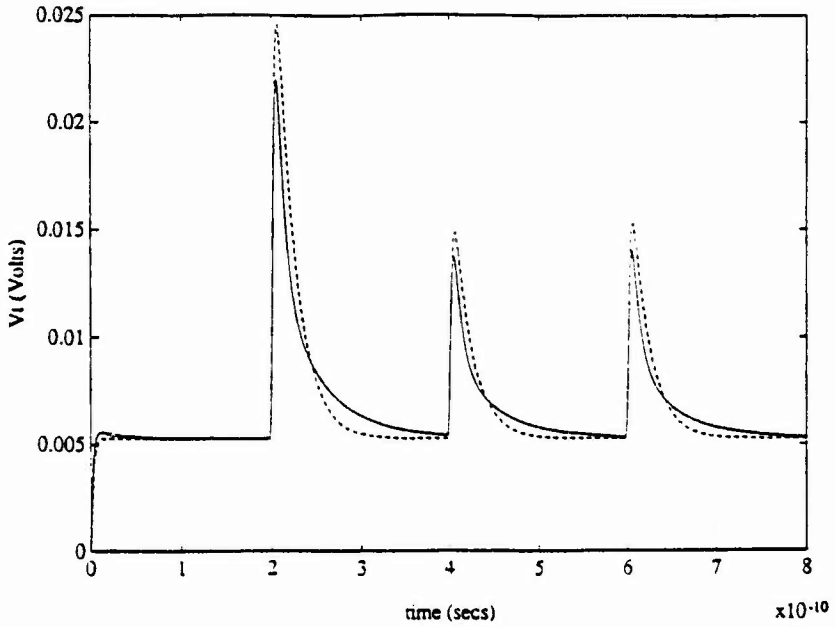

Figure 5: Temporal response of the photoconductive AND device, without electron trapping (dashed), and with electron trapping (solid).

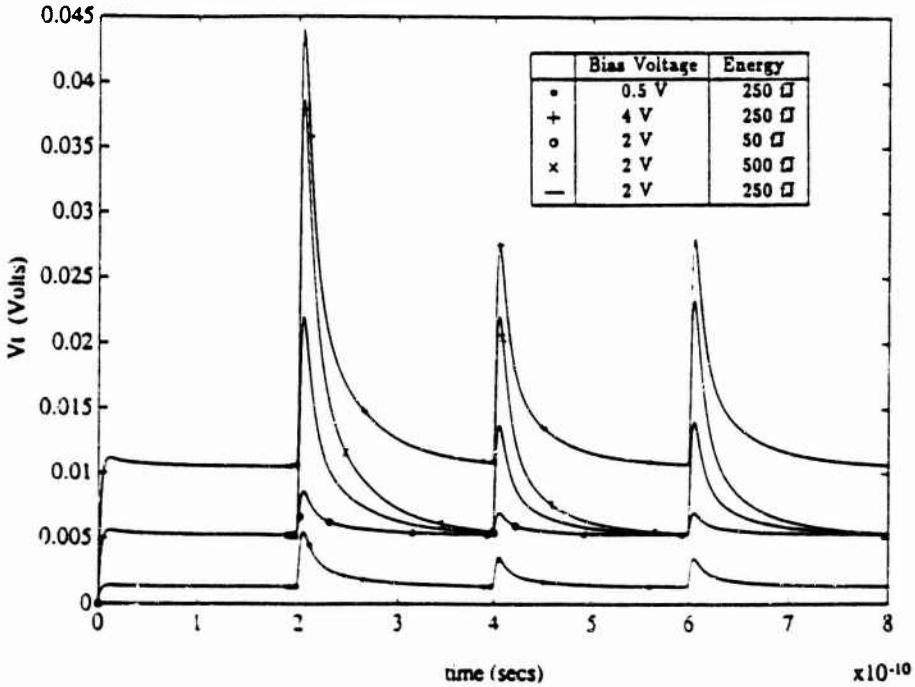

Figure 6: Temporal response of the photoconductive AND device for different values of laser energy and bias voltage.

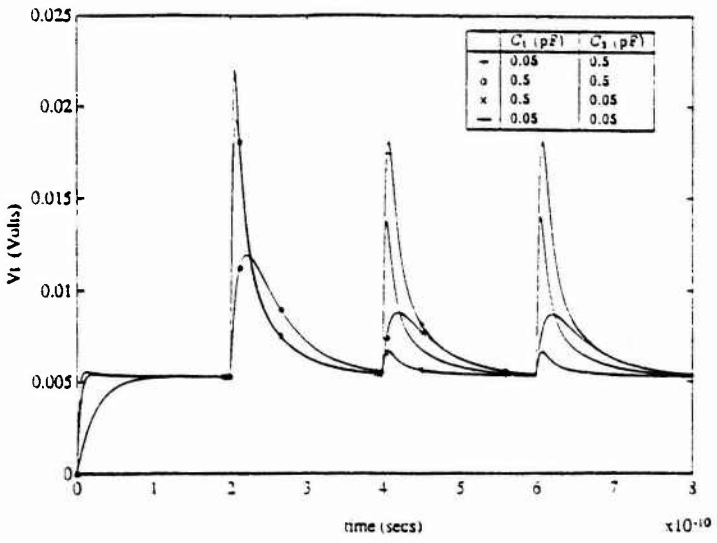

Figure 7: Temporal response of the photoconductive AND device for different values of capacitance.

dc components (leakage currents) increase with bias voltage as expected. Again, the contrast ratio for the AND device is approximately 2:1 in all cases.

Keeping all conditions the same except for the capacitance of the two gaps, a comparison is shown in Fig. 7 for the cases ($C_1 = 0.05$ pF, $C_2 = 0.5$ pF), ($C_1 = 0.5$ pF, $C_2 = 0.05$ pF), and ($C_1 = C_2 = 0.5$ pF).

The fixed contrast ratio of 2:1 can also be explained by examining the form and symmetry of equations (5), (6), and (7). Here the equal contribution of $Q_1(t)$ and $Q_2(t)$ to the total voltage drop across the device is evident. Increasing the capacitance of both detectors lowers and broadens the pulses but the contrast ratio is still 2:1. An asymmetry in capacitance changes the relative response of the (1,0) and (0,1) states but overall the contrast ratio deteriorates. Reducing the capacitance of both gaps improves the frequency response but does not improve the contrast ratio unless the capacitive impedance $1/\omega C$ becomes much larger than the resistance. In this case, the AND device would then be modeled by two resistors connected in series, resulting in contrast ratios other than 2:1.

In summary, a simple but accurate model for the photoconductive AND gate has been developed. Simulations using the model agree well with the experimental data and have been useful in understanding the performance and limitations of the optical AND gate. For example, the contrast ratio is fixed at 2:1 because of the device geometry, not material parameters. Alternative device geometries should be explored in order to improve the contrast ratio.

3.2 NLDE Simulation Model of the AND Device

In order to evaluate the performance of the overall OTDMA architecture in question, an appropriate simulation model of the AND device has to be embedded within a larger system. For this purpose, certain nonlinear differential equation (NLDE) solution methods are more amenable than others. Specifically, we had to restrict our focus on models that accept input samples and produce output samples at *regularly spaced* intervals [6], as opposed to typical adaptive step-size methods (e.g., Runge-Kutta above).

We based our simulation model on the state equation representation from (2) through (7) and considered *linear multistep methods*. Despite the superiority of *implicit* methods in terms of accuracy and stability, we focused on *explicit* methods because of their smaller computational burden and their implementation simplicity (see Jeruchim, *et. al* [6] and references within). We applied the second order Adams-Bashforth method (AB2), summarized as

$$y_{k+1} = y_k + \frac{h}{2}(3\dot{y}_k - \dot{y}_{k-1})$$

where h is the time step (or *sampling interval*), y_k is the solution at time k, and the dot denotes time-derivative [6]. According to the AB2 formulation, and excluding trapping effects, the update equations for (2), and (4) through (6) become

$$n_{1,k+1} = n_{1,k} + \frac{h}{2}[3(-\frac{n_{1,k}}{\tau_n} + \frac{O_{1,k}}{\hbar\omega LHW}) - (-\frac{n_{1,k-1}}{\tau_n} + \frac{O_{1,k-1}}{\hbar\omega LHW})] \quad (8)$$

$$n_{2,k+1} = n_{2,k} + \frac{h}{2}[3(-\frac{n_{2,k}}{\tau_n} + \frac{O_{2,k}}{\hbar\omega LHW}) - (-\frac{n_{2,k-1}}{\tau_n} + \frac{O_{2,k-1}}{\hbar\omega LHW})] \quad (9)$$

$$p_{1,k+1} = p_{1,k} + \frac{h}{2}[3(-\frac{p_{1,k}}{\tau_p} + \frac{O_{1,k}}{\hbar\omega LHW}) - (-\frac{p_{1,k-1}}{\tau_p} + \frac{O_{1,k-1}}{\hbar\omega LHW})] \quad (10)$$

$$p_{2,k+1} = p_{2,k} + \frac{h}{2}[3(-\frac{p_{2,k}}{\tau_p} + \frac{O_{2,k}}{\hbar\omega LHW}) - (-\frac{p_{2,k-1}}{\tau_p} + \frac{O_{2,k-1}}{\hbar\omega LHW})] \quad (11)$$

$$Q_{1,k+1} = Q_{1,k} + \tfrac{h}{2}[\ 3(-\frac{Q_{1,k}}{2Z_0C_1} - \frac{Q_{2,k}}{2Z_0C_2} - \frac{Q_{1,k}G_{1,k}}{C_1} + \frac{V_{i,k}}{Z_0}) \\ -(-\frac{Q_{1,k-1}}{2Z_0C_1} - \frac{Q_{2,k-1}}{2Z_0C_2} - \frac{Q_{1,k-1}G_{1,k-1}}{C_1} + \frac{V_{i,k-1}}{Z_0})\ ] \quad (12)$$

$$Q_{2,k+1} = Q_{2,k} + \tfrac{h}{2}[\ 3(-\frac{Q_{2,k}}{2Z_0C_2} - \frac{Q_{1,k}}{2Z_0C_1} - \frac{Q_{2,k}G_{2,k}}{C_2} + \frac{V_{i,k}}{Z_0}) \\ -(-\frac{Q_{2,k-1}}{2Z_0C_2} - \frac{Q_{1,k-1}}{2Z_0C_1} - \frac{Q_{2,k-1}G_{2,k-1}}{C_2} + \frac{V_{i,k-1}}{Z_0})\ ] \quad (13)$$

Equation (1) leads to

$$G_{1,k+1} = \frac{A}{L}(n_{1,k+1}e\mu_n + p_{1,k+1}e\mu_p) + G_0 \quad (14)$$

$$G_{2,k+1} = \frac{A}{L}(n_{2,k+1}e\mu_n + p_{2,k+1}e\mu_p) + G_0 \quad (15)$$

and (7) is implemented as

$$V_{t,k+1} = V_{i,k+1} - \frac{Q_{1,k+1}}{2C_1} - \frac{Q_{2,k+1}}{2C_2} \quad (16)$$

When trapping effects are taken into account, the additional update equations for the negatively charged electron trap concentrations (from (3)) are:

$$n^-_{t\,1,k+1} = n^-_{t\,1,k} + \frac{h}{2}[3(E_n n^-_{t\,1,k} - C_n n_{1,k}(n_t - n^-_{t\,1,k})) - (E_n n^-_{t\,1,k-1} - C_n n_{1,k-1}(n_t - n^-_{t\,1,k-1}))] \quad (17)$$

$$n^-_{t\,2,k+1} = n^-_{t\,2,k} + \frac{h}{2}[3(E_n n^-_{t\,2,k} - C_n n_{2,k}(n_t - n^-_{t\,2,k})) - (E_n n^-_{t\,2,k-1} - C_n n_{2,k-1}(n_t - n^-_{t\,2,k-1}))] \quad (18)$$

and (2) yields

$$n_{1,k+1} = n_{1,k} + \frac{h}{2}[3(-\frac{n_{1,k}}{\tau_n} + \frac{O_{1,k}}{\hbar\omega LHW}) - 3((E_n n^-_{t\,1,k} - C_n n_{1,k}(n_t - n^-_{t\,1,k})) \quad (19)$$

$$-(-\frac{n_{1,k-1}}{\tau_n} + \frac{O_{1,k-1}}{\hbar\omega LHW}) + (E_n n^-_{t\,1,k-1} - C_n n_{1,k-1}(n_t - n^-_{t\,1,k-1}))] \quad (20)$$

$$n_{2,k+1} = n_{2,k} + \frac{h}{2}[3(-\frac{n_{2,k}}{\tau_n} + \frac{O_{2,k}}{\hbar\omega LHW}) - 3((E_n n^-_{t\,2,k} - C_n n_{2,k}(n_t - n^-_{t\,2,k})) \quad (21)$$

$$-(-\frac{n_{2,k-1}}{\tau_n} + \frac{O_{2,k-1}}{\hbar\omega LHW}) + (E_n n^-_{t\,2,k-1} - C_n n_{2,k-1}(n_t - n^-_{t\,2,k-1}))] \quad (22)$$

We implemented these update equations directly into our simulation model.

The integration time step h is crucial for the stability and accuracy of the solution. In choosing h we used the following heuristic method [6]: Compare solutions using time steps h and $h/2$ and accept the solution if the error for both time steps is within acceptable tolerance. If the error is too large or too small, increase or decrease appropriately the time step, until an appropriate time step is found.

When simulating a device governed by NLDE as part of a larger communication system, the step size required to yield acceptable stability and accuracy may be much smaller than that dictated strictly by aliasing (i.e., bandwidth) considerations. Since the duration of simulations depends directly on the sampling interval, this may impose severe computational limitations, especially if the entire simulation is controlled by a single time step. A typical solution to this problem is to use, whenever possible, a smaller time step internally within the device, and a longer time step for the entire system. This is referred to as *multirate* simulation. In our case, we had to use an internal time step 20 times smaller than the external time step, in order to maintain acceptable stability and accuracy for the AND device model and at the same time keep the total computation requirements for the entire OTDMA system within acceptable limits. For this multirate implementation, we used linear interpolation at the input of the AND device and simple decimation at its output.

4 Alterative Modeling using Artificial Neural Networks

4.1 Simulation Modeling of Nonlinear Devices

Many devices and subsystems in communications can be modeled by nonlinear differential equations (NLDE):

$$\phi[y(t), \dot{y}, \ddot{y}, \ldots, y^{(k)}(t)] + x(t) = 0$$

where $y(t)$ is the output and $x(t)$ is the input of the device or subsystem. Following the discussion in [6], after isolating the highest derivative

$$y^{(k)}(t) = \phi[y(t), \dot{y}, \ddot{y}, \ldots, y^{(k-1)}(t)] + x(t)$$

we can formulate the state equations

$$q_1 = y$$

$$q_2 = \dot{y}$$

$$\ldots$$

$$q_k = y^{(k-1)}$$

that lead to the generalized form

$$\dot{\mathbf{q}} = \mathbf{f}(\mathbf{q}) + \mathbf{x} \tag{23}$$

This also allows for multiple input devices or subsystems. In discrete time, the interval $[0, T]$ is subdivided into a set of sampling points

$$t_0 = 0, \quad t_N = T, \quad t_{n+1} = t_n + h, \quad n = 0, 1, \ldots, N$$

In order to evaluate the performance of the overall communication architecture being studied, an appropriate block simulation model of such devices has to be embedded within a larger system simulation. For this purpose, certain NLDE solution methods are more amenable than others. Specifically, focus is restricted to models that accept input samples and produce output samples at *regularly spaced* intervals [6], as opposed to typical adaptive step-size methods (e.g., Runge-Kutta). *Linear multistep methods* [13, 14] are most often used in such cases:

$$\mathbf{q}_{n+1} = \sum_{i=0}^{p} a_i \mathbf{q}_{n-i} + h \sum_{i=-1}^{p} b_i \dot{\mathbf{q}}_{n-i}$$

where a_i, b_i and the order p define the type of integration formula. Multistep methods can be *explicit* or *implicit* (see [6] and references within for details).

The integration time step h is crucial for the stability and accuracy of the solution. The following heuristic method can be used in choosing h [6]: Compare solutions using time steps h and $h/2$ and accept the solution if the error for both time steps is within acceptable tolerance. If the error is too large or too small, increase or decrease appropriately the time step, until an appropriate time step is found.

When simulating a device governed by NLDE as part of a larger communication system, the step size required to yield acceptable stability and accuracy may be much smaller than that dictated strictly by system-wide aliasing (i.e., bandwidth) considerations. Since the duration of simulations depends directly on the sampling interval, this may impose severe computational limitations, especially if the entire simulation is controlled by a single time step. A typical solution to this problem is to use, whenever possible, a smaller time step internally within the device, and a longer time step for the entire system. This is referred to as *multirate* simulation. Multirate operation involves converting to a higher sampling rate at the input of a subsystem (*interpolation*), and accordingly converting to a lower sampling rate at the output of the subsystem (*decimation*). Of the two operations, decimation is simple but interpolation can be considerably more difficult, the main difficulties lying with the design of the interpolating filter [15, 16].

As mentioned above, detailed differential equation models can be too time consuming to be useful in a system simulation where the nonlinear device is just one of many subsystems. For simulation applications nonlinearities are more efficiently represented as a functional relationship or in tabular form. The authors in [6] refer to such input-output-type models as *nonlinear block models*, generally divided in two groups, *instantaneous* or *memoryless models* and *models with memory*.

Due to the computational burden, the increased complexity, and the stability problems imposed by directly simulating the NLDE, it is often desirable to compute and implement non-NLDE based models. Such models are basically explicit input-output nonlinear systems with memory:

$$y_n = g(x_n, x_{n-1}, \ldots, x_{n-M+1})$$

where, for practical purposes, the memory length M is assumed finite. These models require some computation up-front (before the simulation) and trade off some accuracy for increased stability and reduced complexity during the simulation. The obvious advantage for such representations is that they operate at the *lower*, system-wide sampling rate, instead of the much higher device rate that a NLDE-based model requires. Furthermore, in most cases, they do not introduce solution stability problems. Finally, if chosen properly, the number of arithmetic operations they require per time step, can be significantly smaller.

Some common simulation modeling strategies involving block models with and without memory, both baseband and bandpass, are described in [6]. Block models for specific communication devices and subsystems such as TWT amplifiers and phase-locked loops (PLL) are also discussed in [6].

One family of such models are those based on the Volterra or the Wiener series [7]. Approximate Volterra models of finite order and memory can be constructed by collecting a series of input-output samples from the original device (e.g., from the NLDE) and then solving a system of equations, or in some cases, directly from the differential equation description of the original system [8].

Another general way to represent systems, both linear and nonlinear, is the Kolmogorov-Gabor polynomial [17] shown below:

$$y = a_0 + \sum_i a_i x_i + \sum_i \sum_j a_{ij} x_i x_j + \dots \tag{24}$$

where y is the output and x is the input to the system. Gabor *et al.* [17] proposed a learning method that adjusted the coefficients of (24) by minimizing the mean square error between each desired output sample and the actual output. A similar approach has been presented in [18].

As noted in [9], the approaches described above suffer from the rapid explosion of the possible combination of terms as the order of the polynomial increases. The number of samples needs to be very large, which for practical purposes can be difficult to achieve. They also require repeated presentation of the training data or infinite sequences.

In the multivariable case, beside the increased complexity of the formulation one also has to cope with the dramatically increasing computational burden in training as well as in on-line simulation run time required by such models.

In the following section we focus on another interesting modeling paradigm involving *artificial neural networks.*

4.2 Application of Feed-Forward ANN

Artificial neural networks (ANN) are emerging as a computational technology with the potential of a significant contribution to many application areas. Current applications range from pattern recognition to optimization and scheduling [19]. Although still a field of very active research, ANN are now entering a phase of a certain maturity, in software and hardware implementation aspects, as well as in the domain of mathematical formalization.

As a generic definition, an ANN is a highly interconnected computational network specified by three elements, namely a set of processing elements (nodes or "neurons"), a topology of weighted connections between these elements, and a learning law for updating the connection weights. There are several types of neural networks, with different structure, dynamics and learning methods, and with different strengths particular to their application. Here, keeping the large number of available neural network structures and learning rules in mind, we restrict our attention to feed-forward, back-propagation ANN and their application to the efficient simulation of communication systems. More sophisticated neural network architectures and learning algorithms could certainly also be considered, with potential additional advantages. However, that remains as the subject of future work.

An example of a simple, one-hidden-layer, feed-forward ANN is shown in Fig. 8. Based on the *back-propagation* training algorithm such networks can be trained using correct input-output patterns to represent virtually any nonlinear function [20, 21, 22].

An application area of specific interest to the communications systems engineering field is that of function approximation, taking the form of system identification tech-

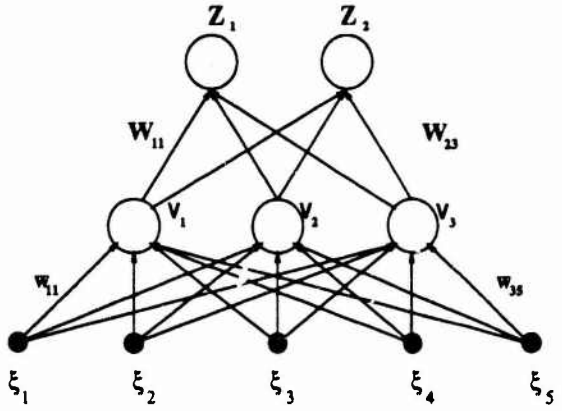

Figure 8: An example of a one-hidden-layer, feed-forward ANN. W_{jk} and w_{ij} are connection weights, ξ_k's denote inputs, Z_i's denote outputs, and V_j's denote the outputs of the hidden nodes.

niques (see the recent papers [10, 23, 24, 25] and references within). Furthermore, neural networks can be used not only to identify but also to control dynamical systems [10, 11]

Our focus here is not on control but on *simulation* of communication systems. We discuss here an alternative modeling and simulation paradigm that involves ANN. We propose ways to exploit the large amount of existing network architectures and learning methods in order to improve the simulation efficiency of communication systems involving nonlinearities. Whereas recent work has focused on the use of ANN for the identification and control of dynamical systems, we focus on using ANN to identify nonlinear systems for simulation purposes. The growing wealth of neural net structures and techniques presents an appealing family of modeling tools to the simulation practitioner.

The underlying idea is to train a neural net to "mimic" the behavior of nonlinear device or subsystem. To avoid the multirate problems of the NLDE-based blocks, the ANN block model has to operate at the lower, system-wide sampling rate. The ANN block model can also possess memory in the form of tapped-delay lines, one per block input. Training patterns can be obtained from the standard numerical solution to the NLDE, or from experimental measurements, and training can take place using back-propagation techniques, until the desired degree of matching between the required and the actual output of the network is obtained.

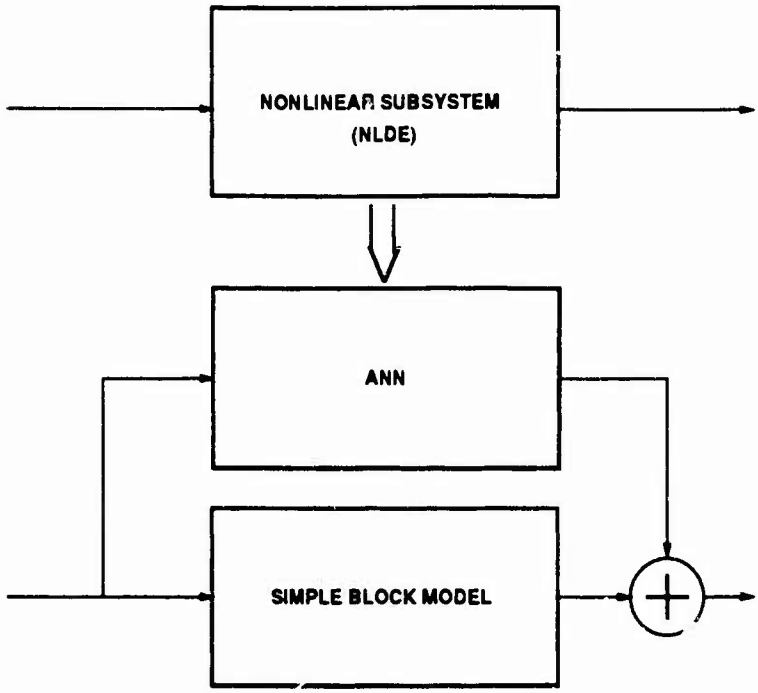

Figure 9: Schematic illustration of use of ANN in parallel to a simple block model, in order to compensate for residuals.

An ANN can also be used to improve the simulation accuracy of simple block models. In many cases, based on *a priori* knowledge or experience, we can start the modeling process by approximating the given subsystem by a simple, computationally efficient block model, say an FIR linearity or a memoryless nonlinearity followed by a linear system or another simple combination of linear and nonlinear blocks. In such cases, initial analysis may show that although some operational characteristics of the original device are preserved other characteristics are not. One way to compensate for the residuals (i.e., differences) while maintaining computational efficiency is to use an ANN "in parallel" to the simple block model, as illustrated in Fig. 9. Such an ANN can potentially be kept at minimum size and memory requirements while significantly improving the overall accuracy by approximating the residuals. This is further supported by our empirical observations in Section 5.

4.3 Issues and Comparisons

We compare here the neural net-based simulation approach to the linear multistep (LM) integration technique, in terms of application complexity and simulation efficiency. We base the comparison and trade-off study on a multilayer feed-forward ANN. Similar analyses can be performed for other types of ANN. Our comparison examines computational burden as well as accuracy and stability issues.

Here we assume that an accurate NLDE model already exists. Clearly, in cases where such a model is not readily available, and where direct training data can be obtained efficiently, the ANN-based approach has many additional advantages.

4.3.1 Runtime

Any run time comparison between the two alternative approaches has to include both computational requirements during the system-level simulation, and computational overhead *before* system-level simulations are performed, in order to construct the device or subsystem model.

Clearly, no "off-line" computational overhead is involved when using the direct differential equation integrator, except maybe for the time required by the trial-and-error process to find the maximum acceptable time step h. A block model for the subsystem in question can be constructed directly based on the standard approach described in [6]. On the other hand, the ANN-based block model has to be appropriately trained before system simulations are run. Such training would typically involve generating a number of "correct" input-output patterns from the corresponding differential equation model or experimental measurements, and executing the back-propagation learning algorithm until acceptable accuracy (usually measured in terms of a normalized mean-squared error) is obtained. The number of learning iterations (training epochs) required depends in general on the nonlinear operation performed by the subsystem in question.

The strength of the ANN-based block model is mainly in the actual system-level simulation run time, as illustrated by the following approximate analysis: A feed-forward

ANN with L hidden layers, N_i nodes in the ith hidden layer, I inputs and O outputs requires

$$IN_1 + \sum_{i=1}^{L-1} N_i N_{i+1} + ON_L$$

multiplications

$$(I-1)N_1 + \sum_{i=1}^{L-1}(N_i - 1)N_{i+1} + O(N_L - 1)$$

additions, and

$$\sum_{i=1}^{L} N_i + O$$

calculations of the sigmoidal function per output sample. Assuming that each sigmoidal calculation is equivalent to S multiplications, the total number of multiplications becomes

$$IN_1 + \sum_{i=1}^{L-1} N_i N_{i+1} + ON_L + S(\sum_{i=1}^{L} N_i + O)$$

Denote the total number of calculations above by T_{ANN}.

Let us assume that state equation (23) involves the equivalent of N_M multiplications and N_A additions. Then, using the explicit second order Adams-Bashforth method as an example, the LM numerical integration method requires

$$2N_M + 3$$

multiplications and

$$2N_A + 2$$

additions per time step h. Denote the resulting total number of calculations per internal time step by T_{LM}. Other explicit methods involve a similar number of operations, while most *implicit* methods require many more operations per time step, since they also include the solution of a set of nonlinear equations per step (requiring evaluation of Jacobians, etc.).

Assume further that the solution to the differential equation requires a time step h that is R times smaller than an acceptable system-wide sampling interval T_s. Denote the

number of calculations required to simulate the rest of the system by T_{SYS} per output sample. There are again two cases: If we elect not to employ multirate sampling when using the differential equation model, the overall system has to be simulated at a rate of $1/h$. The efficiency improvement of the ANN implementation over the LM method then becomes

$$R_1 = \frac{R(T_{LM} + T_{SYS})}{T_{ANN} + T_{SYS}} \tag{25}$$

with $R_1 \approx R$ when $T_{SYS} \gg T_{ANN}$ and $T_{SYS} \gg T_{LM}$.

In the second case, when multirate sampling is employed, the efficiency improvement becomes:

$$R_2 = \frac{R(T_{LM} + T_{IP}) + T_{SYS}}{T_{ANN} + T_{SYS}} \tag{26}$$

where T_{IP} is the additional computation due to the use of the interpolation filter at the input of the differential equation block model.

When, as suggested in Section 3, the ANN is used "in parallel" with another block model (e.g., an FIR filter) requiring computation T_{BM}, (26) becomes

$$R_2 = \frac{R(T_{LM} + T_{IP}) + T_{SYS}}{T_{BM} + T_{ANN} + T_{SYS}} \tag{27}$$

From the above equations we see that the ANN implementation is clearly more efficient in the first case, while in the latter cases it still has the potential of being more efficient when $R \gg 1$, T_{BM} is small, and $RT_{LM} > T_{ANN}$.

4.3.2 Accuracy and Stability

Taking the solution to the set of differential equations as the "correct" response of the subsystem in question, the LM methods can exhibit superior accuracy, given an appropriately chosen time step h. Their appealing characteristic is that they allow for a more direct control of truncation error, via the choice of integration method and time step, as opposed to the ANN implementation whose behavior is based on the anticipated "generalization" of the network's training.

However, LM methods can be affected by stability problems, related to the propagation and growth of error at successive time points [6, 26]. In general, stability will depend both on the integration method and the problem. In contrast, the ANN approach does not introduce solution stability problems.

4.3.3 Overall Comparison

In terms of generality and robustness of the simulation approach, ANN offer an attractive alternative to standard NLDE implementation algorithms, that avoids the issues of sampling rate and stability, possibly in exchange for a somewhat reduced accuracy. LM solutions can be both accurate and stable *for a small enough* h, while ANN implementations trade off some accuracy for simulation speed and immunity versus stability problems.

In terms of simulation run time we observe the following: At the device level, the above analysis indicates that unless the state equations of the nonlinearity are extremely simple, the ANN block model is more efficient (after training).

At the system level, a comparison is meaningful only if multirate sampling is used, otherwise the system model including the ANN block is much more efficient, as indicated by (25).

When multirate sampling is used, one has to consider the savings per output sample described by (26) or (27) multiplied by the length of the required simulations times the number of anticipated repetitions versus the overhead involved in initially training the ANN. This is summarized in the overall efficiency improvement ratio

$$R_3 = \frac{N_R\, N_S\, [R(T_{LM} + T_{IP}) + T_{SYS}]}{N_R\, N_S\, [T_{BM} + T_{ANN} + T_{SYS}] + T_{TR}} \tag{28}$$

where N_S is the number of samples per simulation run, N_R is the number of repeated runs, $T_{BM} = 0$ if the ANN is used alone, and T_{TR} is the computational cost of training the ANN block model. Clearly, if the savings in (26) or (27) are significant and if the block model in question is going to be used extensively in repeated simulations, the trade-off between training and run time savings expressed by (28) can dramatically favor the use of the ANN-based models.

4.4 ANN for OTDMA System Simulation

The AND device is modeled using the differential equations given earlier, with $L = 5$ μm, $W = 5$ μm, $H = 1.4$ μm, $\mu_n = 6{,}000$ cm^2/Vs, $\mu_p = 300$ cm^2/Vs, $\tau_n = \tau_p = 20$ ps, $1/G_0 = 19$ kΩ, $n_t = 10^{15}$ cm^{-3}, $C_n = 10^{-5}$ s^{-1}, $E_n = 5 \times 10^{10}$ cm^3/s, $C_1 = C_2 = 0.05$ pF, $Z_0 = 50$ Ω, and $V_i = 2.0$ V. For improved accuracy and stability the AND device uses an internal time step of 0.25 ps.

To construct an ANN-based computation model for the AND device, we assume that the device can be modeled reasonably well as a nonlinear device with finite memory. We then have to decide on the fixed memory length, M (that also determines the number of inputs to the ANN), as well as the structure of the ANN to use (number of layers, number of nodes in each layer, etc.). We use hidden nodes with sigmoidal nonlinearity and a linear output node. Then a number of input vectors (each vector a number of samples equal to the memory length, one vector for each device input) and corresponding output samples have to be obtained for regularly spaced intervals, using the numerical solution of the NLDE. The network is trained using the back-propagation algorithm, until an acceptably low mean square error (MSE) between the required and the actual output of the network is obtained. After training, the network weights are fixed and the ANN takes the place of the AND device in the simulation, using a tapped-delay line for each device input port to feed input samples corresponding to times $k, \ldots, k - M + 1$ to the network, at each time instant k. Therefore, at each time k the network uses $2 \times M$ input samples to produce an output sample.

Here we use single hidden layer ANN with 40 input nodes (memory $M = 20$ per device input) and 10 hidden nodes.

As an example of another modeling approach, we also approximate the behavior of the AND device (with charge trapping effects not taken into account) by the summation of two FIR filters (one for each device input) and an ANN "in parallel" that compensates for the residual error, as shown in Fig. 10. For our example, we chose the FIR filters to have $M_{FIR} = 34$ taps, based on the "impulse response" of the AND device (the output

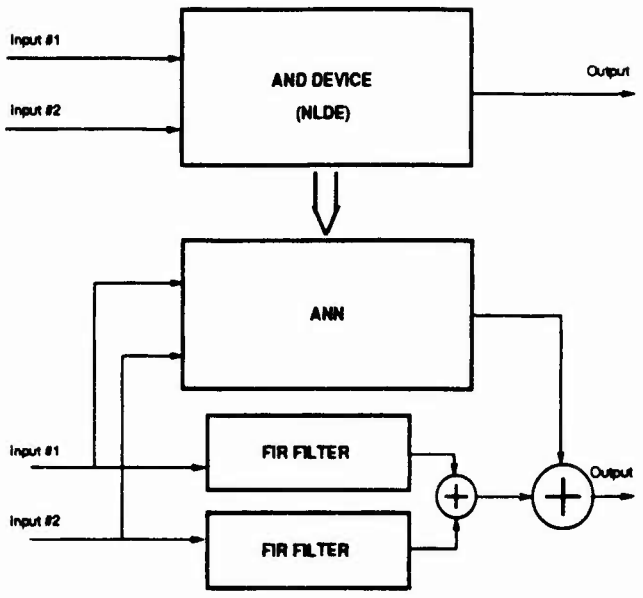

Figure 10: Simulation block model of the AND device as the summation of two FIR filters (one for each device input) and an ANN that compensates for the residual error.

of the device when an impulse is applied to one input while no signal is applied to the other input). Therefore

$$T_{BM} = 2 \times 34 + 2 \times 33 + 2$$

Figures 11 and 12 both illustrate the accuracy of the ANN-based models. Fig. 11 compares the output of the NLDE solution versus the output of the trained ANN for a series of input impulses different from those used for training. Fig. 12 compares the output of the NLDE solution versus the output of a two-input FIR system plus that of of the trained "parallel" ANN, for the same series of input impulses used for training.

In all cases, we used 165 training input-output patterns, taken from a time interval of 1000 ps in the response of the device to a series of impulses applied to its inputs. Training was stopped in each case when additional iterations did not significantly reduce the training MSE, typically after about 4,000 epochs.

We have restricted our focus to a simple network and learning algorithm in order to demonstrate the principle of the methodology. Recent research in neural networks offers methods to reduce network size to a minimum and thereby reduce computational

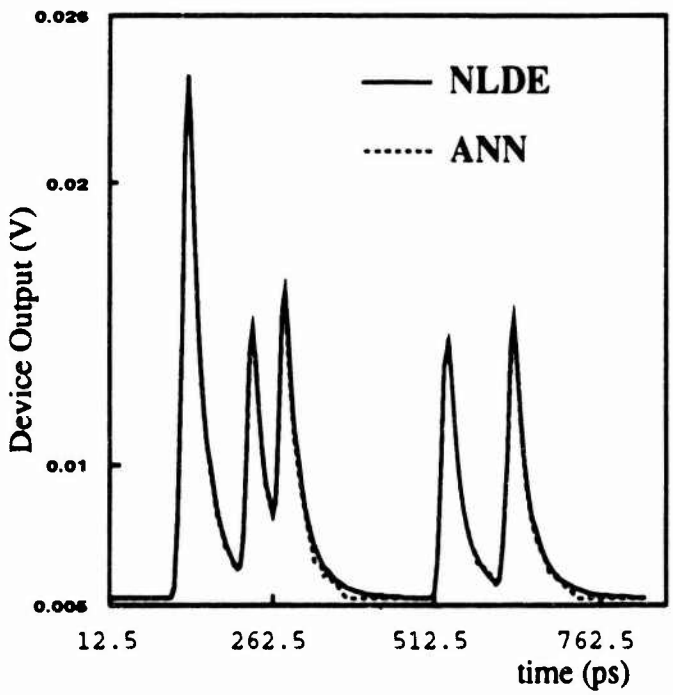

Figure 11: To illustrate the accuracy of the ANN-based model we plot the output of the NLDE solution versus the output of the trained ANN for a series of input impulses different from those used for training.

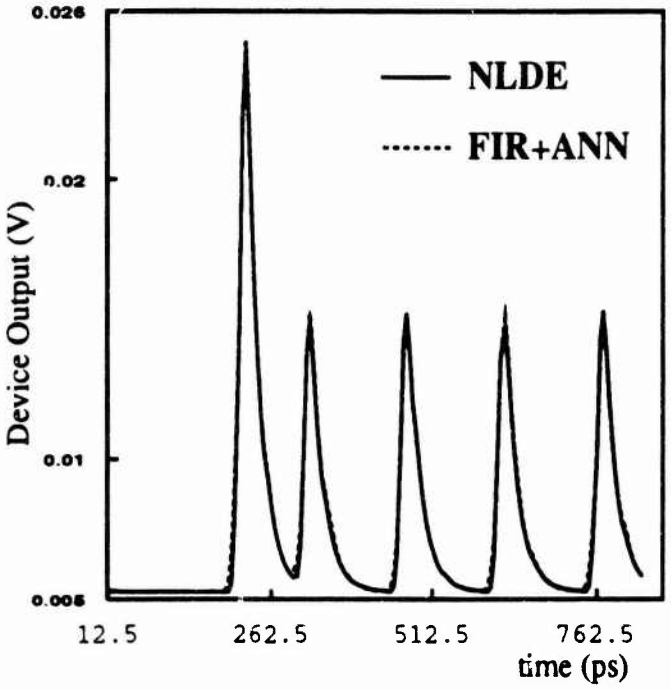

Figure 12: To illustrate the accuracy of the second ANN-based model we plot the output of the NLDE solution versus the output of a two-input FIR system plus that of of the trained "parallel" ANN, for the same series of input impulses used for training.

	ANN $M = 20$ 40 Input Nodes 10 Hidden Nodes (No Trapping)	ANN $M = 20$ 40 Input Nodes 10 Hidden Nodes (Trapping)	FIR $M_{FIR} = 34$ (No Trapping)	FIR + ANN $M = 10$ 20 Input Nodes 8 Hidden Nodes (No Trapping)
Runtime per Epoch	0.6 s	0.6 s	–	0.3 s
Test NMSE	8.78×10^{-4}	8.39×10^{-4}	4.1×10^{-3}	7.74×10^{-4}
Addition Ratio	1.95	3.12	10.96	3.41
Multiplication Ratio	4.12	5.36	31.2	6.6

Table 1: Runtime per training epoch, resulting accuracy, and computational requirements for the ANN-based models. The last two rows give the ratio of numerical operations required by the NLDE model over the numerical operations required by the respective block model, per system-wide (i.e., external) time step. For comparison, we include the case where the combined FIR filters alone approximate the behavior of the AND device (M_{FIR} is the number of taps in each FIR filter.)

overhead and improve generalization (i.e., improve simulation accuracy on new data) [40, 41, 42]. In addition, cross-validation techniques can be used to determine the optimal time to stop training. With this technique, training is completed when the error on a separate test set just starts to increase [43]. Methods for improving generalization are particularly valuable when the training data are "noisy" *and* there is not a great deal of training data available.

The required run time per training epoch, the resulting accuracy, and the computational requirements for the ANN-based models are shown in Table 1. The *normalized mean-square error* (NMSE) is the MSE divided by the mean-square value of the test patterns. Table 1 also includes the ratio of numerical operations required by the NLDE model over the numerical operations required by the ANN model, per system-wide (i.e., external) time step. This ratio gives an indication about the run time speed-up factor obtained when using the corresponding ANN-based model. In the table, we included the case where the combined FIR filters alone approximate the behavior of the AND device.

In our multirate implementation the simple linear interpolation and decimation added

another 4 multiplications and 3 additions per *internal* time step h, hence

$$T_{IP} \approx 0.035 T_{LM}$$

when charge trapping effects are included in the device model, and

$$T_{IP} \approx 0.049 T_{LM}$$

when charge trapping effects are not included. An approximate expression for the number of calculations performed for the OTDMA simulation model is found to be

$$T_{SYS} \approx 0.85 T_{LM}$$

and

$$T_{SYS} \approx 1.19 T_{LM}$$

for the two cases above, respectively.

Taking into account the multirate ratio $R = 20$, equations (26) and (27) yield the results in Table 2 showing RT_{LM}/T_{ANN}, R_2, and the experimentally determined R_2 for each case. Here, an addition is assumed to take as much run time as a multiplication, and a calculation of the exponential function (required in the sigmoidal nonlinearity of the ANN nodes) is assumed to take 8.5 times longer than a multiplication. These results agree well (also considering computational overhead in the block simulation package) with our experimental comparison of run times between the OTDMA system simulation using the NLDE block model and the OTDMA simulation using the ANN block model.

Based on the parameter values above, and on the experimentally measured values of R_2, Fig. 13 shows the speedup ratio R_3 versus the total number of receiver decisions, for three cases: Memory of 20, 10 hidden nodes, NLDE with charge trapping effects; memory of 20, 10 hidden nodes, NLDE without charge trapping effects; and ANN parallel to FIR filters, memory of 10, 8 hidden nodes, NLDE without charge trapping effects. In all cases, the ANN-based models result in efficiency improvement over the standard NLDE numerical integration when more than 1,000 or 2,000 receiver decisions are involved. Such a number of simulated decisions is rather common, e.g. when estimating bit error rates (BER) of less than 10^{-2}.

	ANN $M = 20$ 40 Input Nodes 10 Hidden Nodes (No Trapping)	ANN $M = 20$ 40 Input Nodes 10 Hidden Nodes (Trapping)	FIR + ANN $M = 10$ 20 Input Nodes 8 Hidden Nodes (No Trapping)
RT_{LM}/T_{ANN}	3.16	4.37	5.26
R_2	2.95	3.97	3.73
Measured R_2	2.325	2.75	3.169

Table 2: RT_{LM}/T_{ANN}, R_2, and the experimentally determined R_2 for the ANN-based models in Table 1.

5 OTDMA Network Performance Analysis

We now turn our attention to performance analysis of the OTDMA network as an entire entity. Both analytical and simulation -based techniques are used to evaluate performance of the network as a function of device and subsystem parameters.

5.1 Crosstalk Analysis

The effect of crosstalk from adjacent channels (or slots) in the OTDMA frame using a photoconductive AND device with noninfinite contrast ratio for demultiplexing is presented in this section. A block diagram of the receiver showing the photoconductive AND device, pre-amplifier, I&D filter, and decision functions are shown in Fig. 1. Assuming integer integration time-intervals, pulse widths which are less than the slot time T_s (no intersymbol interference, or ISI), and ideal timing in the receiver, it is possible to analytically determine the BER due to crosstalk, neglecting all other noises and degradations. Including other impairments would complicate the analysis and require Monte Carlo simulation, as discussed in a later section.

Let the integration time interval for the I&D filter following the AND device be defined as I, where I is an integer number of slots. We let R denote the contrast ratio, and A be the integrator output over one slot assuming a coincident 1 and 0. The value of A is determined by the amount of leakage current in the AND device, i.e., noninfinite contrast

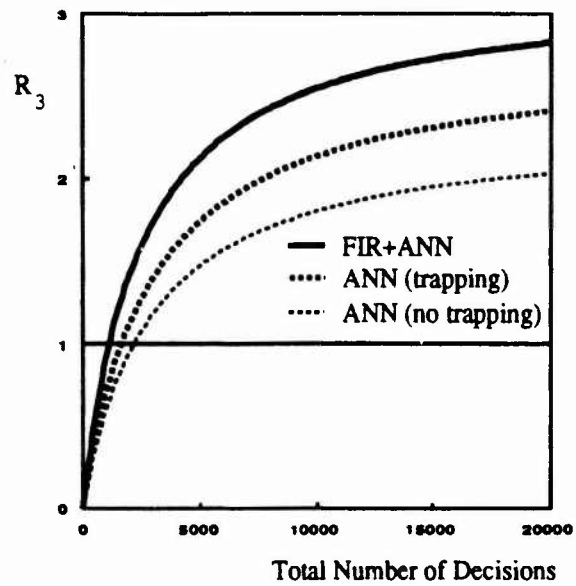

Figure 13: Speedup factor R_3 versus the total number of receiver decisions, for three cases: Memory of 20, 10 hidden nodes, NLDE with charge trapping effects; memory of 20, 10 hidden nodes, NLDE without charge trapping effects; and ANN parallel to FIR filters, memory of 10, 8 hidden nodes, NLDE without charge trapping effects.

ratio. Thus, the I&D output for coincident 1's would be given by RU. A truth-table for the AND device under these assumptions is shown in Table 3. Note that this table assumes no timing offset between the two input optical pulse signals.

In a photoconductive AND device with finite contrast ratio, data in adjacent slots introduces crosstalk and at a minimum reduces the noise margin of the signal at the integrator output. In more severe cases, crosstalk introduces bit errors, even in the absence of other degradations.

Integrating over a larger number of slots (larger I) will increase the deleterious effects of crosstalk. This is in conflict with the constraint that the electrical processing of the detected signal should ideally not require processing at the large aggregate bandwidth of the network. Translating this constraint to the design of the I&D filter requires that the integration time interval (I slots) should be made as large as possible — preferably equal to the frame interval $T = NT_s$. This would also greatly simplify the timing requirements of the receiver.

Data	Clock	Integrator Output
0	0	0
0	1	U
1	0	U
1	1	RU

Table 3: Truth-table for photoconductive AND device with leakage, for all combinations of coincident 1's and 0's. The third column gives the output of the I&D filter following the AND device. The integration interval is one slot.

Thus, there exists a tradeoff between the integration time interval and the contrast ratio R required to ensure a minimum level of BER performance. In this section we derive the minimum contrast ratio of the AND device, R_{min}, that ensures no errors due to crosstalk for a given I.

Within a frame, the I&D filter output $y(t)$ is given by

$$y(t) = \int_{t_0}^{t} x(\alpha) d\alpha \tag{29}$$

where $x(t)$ is the I&D input signal and t_0 is the start time of integration.

A decision is made each frame by comparing $y(T_d)$ to a decision threshold level θ, where T_d is the decision time at the end of the integration period, immediately before the integrator is reset. The BER at the output of the I&D filter is given by

$$\text{BER} = \frac{1}{2} P[y_0(T_d) < \theta] + \frac{1}{2} P[y_1(T_d) > \theta] \tag{30}$$

where the "0" and "1" subscripts denote conditioning of $y(T_d)$ on a transmitted data bit equaling 0 or 1, respectively. Equiprobable 0's and 1's are assumed.

The value R_{min} to ensure no bit errors due to crosstalk can be determined by considering the worst-case, noiseless, minimum separation condition between the two sets of I&D output amplitudes corresponding to transmitted 0 and 1 data bits, respectively. Assuming that the integration interval is an integer number of slots, I, this minimum separation condition occurs when the desired channel data bit equals 0 with the $I - 1$

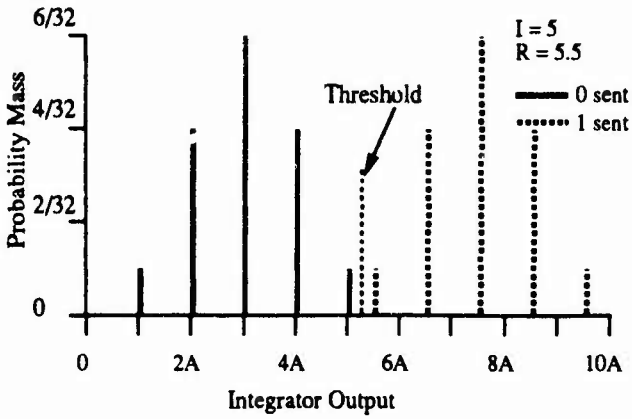

Figure 14: Conditional probability mass functions of the integrator output, $y(T_d)$ conditioned on a transmitted 0 and transmitted 1 in the desired channel. The integration interval is 5 slots and the contrast ratio is 5.5.

adjacent channel data bits all equal to 1, and when the desired channel data bit equals 1 with the $I-1$ adjacent channel data bits all equal to 0. Of course, other crosstalk bit patterns are possible, and the conditional probabilities of occurrence of these patterns can be calculated. The conditional probabilities corresponding to the possible output levels of the I&D filter for the specific case of $I = 5$ are shown in Fig. 14. The contrast ratio in Fig. 14 is 5.5.

As can be seen from the figure, the maximum value for $y_0(T_d) = IU$ and the minimum value for $y_1(T_d) = RU$. Thus, to guarantee unambiguous detection in the noiseless case, $\max\{y_0(T_d)\} < \min\{y_1(T_d)\}$, thus requiring

$$I < R \tag{31}$$

From (31) $R_{min} = I$. This is an important result — for one thing (31) shows that to avoid crosstalk induced bit errors, the contrast ratio must be larger than I, the number of slots in the integration interval of the I&D filter. Since the bandwidth of this filter is inversely proportional to the integration interval, the inequality in (31) sets a minimum bandwidth for error-free performance assuming no noise. Thus, it is desirable for I to be as large as possible (with $I = N$ being the largest value). Note that in this analysis

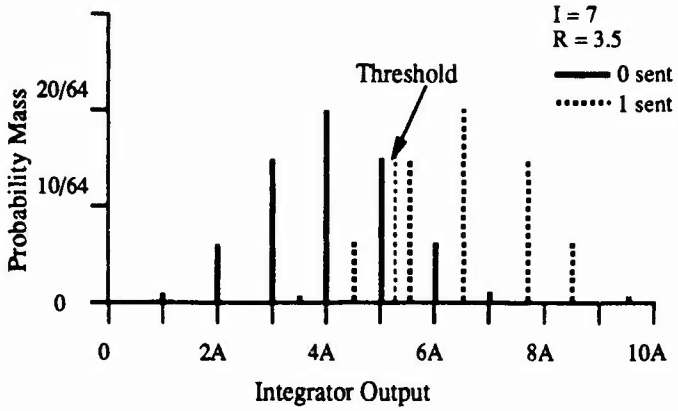

Figure 15: Conditional probability mass functions at the integrator output conditioned on a transmitted 0 and a transmitted 1 in the desired channel with two levels of overlap ($n_v = 2$). The integration interval equals 7 slots.

we only consider the integration time interval in units of integer numbers of slots. The simulation analysis discussed in the sequel investigates integration intervals of arbitrary length. The contrast ratio R is, however, a real number. Therefore, $R = 2.1$ for $I = 2$ would satisfy the inequality.

From this analysis it can be seen that a modest improvement in contrast ratio will not provide significant reduction in the bandwidth required of the I&D filter in the receiver.

5.2 Nonzero Bit Error Rate due To Crosstalk

Violating the inequality in (31) results in bit errors due to crosstalk, even in the absence of noise and other degradations. The net effect is that at least some levels at the I&D output overlap, i.e., cross the decision threshold, and result in errors. If the probability of occurrence of these overlapping levels is sufficiently small, this approach could be exploited to relax the requirement on contrast ratio and integration time interval. We briefly present some results using this idea, and show that it is only feasible for large I.

The conditional probabilities corresponding to the possible integrator output levels for the case $I = 7$ and $R = 3.5$ are shown in Fig. 15. This results in two levels overlapping, thus introducing bit errors due to crosstalk.

I	$R_{min,v}$	BER
50	46	8.8×10^{-14}
20	16	3.8×10^{-5}
7	3	1.1×10^{-1}

Table 4: Table of BER values and minimum contrast ratios for three different values of the parameter I, the integration interval in slots, assuming two integrator output levels overlap ($n_v = 2$).

Once again assuming no timing errors, and that the integration interval is an integer number of slots, I, we can compute the BER due to crosstalk. Realistically assuming that the data bits in the I slots are independent, $y(T_d)$ conditioned on the transmitted data value is a binomially distributed random variable. Let n_v be the number of amplitude values of $y_0(T_d)$ which overlap with values from $y_1(T_d)$. We are still assuming that the I&D filter interval is an integer number of slots I.

Because of the symmetry of the two conditional distributions the BER for the case with overlapping amplitude values is given by

$$\text{BER} = \sum_{k=0}^{n_v-1} \binom{I-1}{k} 0.5^{I-1} \tag{32}$$

assuming no noise, and that the decision threshold is set to an optimal value, given by $\theta = \frac{U}{2}(I+R)$.

The relationship between contrast ratio and n_v is given by

$$I - 2n_v < R < I - 2n_v + 2 \qquad \text{where} \quad I > 2n_v \tag{33}$$

Tabulated in Table 4 are BER values when $n_v = 2$. Thus overlapping output values for the transmitted 1 and transmitted 0 cases does relax the requirements on contrast ratio when compared to the case where there is no overlap (and thus no bit errors due to crosstalk). This can be seen from the inequality in (33). Letting $R_{min,v}$ be the minimum contrast ratio allowed by (33) for a given overlap n_v, we have that $R_{min,v} = R_{min} - 2n_v$. This benefit is achieved at the expense of increasing the BER due to crosstalk.

As can be seen from Table 4, the BER due to crosstalk does not become acceptable until the integration interval is large. Therefore, the contrast ratio must still be very large before this technique is practical.

5.3 Crosstalk in the Tunable Delay

The receiver selects a transmitter by delaying the clock signal to the desired transmitter's slot within a frame. A variable-integer delay line OTDMA coder has been demonstrated experimentally using 2×2 $LiNbO_3$ optical crossbar switches [2]. Crosstalk in the 2×2 sections results in attenuated versions of the clock signal being shifted to all adjacent slots within the frame. Also, the power of the clock pulse in the desired slot is reduced. The net result is a further degradation in performance. Specifically, the crosstalk energy from adjacent slots is increased at the I&D output.

Let γ denote the optical power gain factor in the desired paths within a 2×2 crossbar switch, and β be the crosstalk gain factor. Thus for a signal $c(t)$ at either input port, $\gamma c(t)$ is output at the desired output port, and $\beta c(t)$ is transferred to the other output port, this latter term represents crosstalk.

An m stage switch provides 2^{m-1} possible addresses (delays). One extra switch is used to route the signal to the correct output port. It can be shown that the desired path gain will be $\gamma^m c(t)$, and the crosstalk terms will be of the form $\gamma^k \beta^i c(t - t_l)$, where t_l is a delay corresponding to one of the adjacent slots, and $m = i + k$. Every adjacent slot will contain one of these crosstalk terms.

A worst-case analysis assumes that all adjacent crosstalk terms are set to the largest possible value. For m even, this is $\beta^m c(t)$. For m odd, the largest value for a crosstalk term is $\beta^{m-1}\gamma^1 c(t)$. For the 2×2 $LiNbO_3$ used in the Rome Laboratory demonstration [2] crossbar switch crosstalk power was no[illegible] 20 dB, yielding $\gamma = 0.99$ and $\beta = 0.01$. For the $LiNbO_3$ switch, the net effect on system performance is minimal, but could be significant for devices with more crosstalk, and should be included in the system analysis for these cases.

5.4 Simulation Results

In our implementation of the entire OTDMA architecture we assumed $N = 8$ users (i.e., 8 slots per frame). Laser pulses were modeled as pulses of Gaussian temporal shape, with standard deviation 5 ps, and energy equal to 2.5×10^{-13} J. Both the slot under observation (the 5th slot in our case) and the remaining slots, were assumed to contain binary digits, with 0 and 1 being equiprobable. Information bits for the slot under study and among all slots were assumed independent. The system-wide sampling interval was set to 5 ps, corresponding to 40 samples per slot, and 320 samples per frame.

Losses in the fiber, the passive star and the electro-optic modulator, as well as the tunable delay line cross-talk were incorporated in the laser pulse energy.

As before, the AND device was modeled using the differential equations given earlier, with $L = 5$ μm, $W = 5$ μm, $H = 1.4$ μm, $\mu_n = 6{,}000$ cm^2/Vs, $\mu_p = 300$ cm^2/Vs, $\tau_n = \tau_p = 20$ ps, $1/G_0 = 19$ kΩ, $n_i = 10^{15}$ cm^{-3}, $C_n = 10^{-5}$ s^{-1}, $E_n = 5 \times 10^{10}$ cm^3/s, $C_1 = C_2 = 0.05$ pF, $Z_0 = 50$ Ω, and $V_i = 2.0$ V. The differential equation model was implemented using the AB2 update formulas from above. For improved accuracy and stability the AND device used an internal time step of 0.25 ps.

The receiver consisted of an I&D filter of variable duration, so that the effects of the integration period on the performance of the system could be studied. The same clock pulses used to select the chosen slot at the AND device, were also used to center the integration interval around the required slot. The I&D filter produced one output sample per frame. These output samples were then compared to a threshold θ, to decide whether a 1 or a 0 had been received.

Extensive initial simulation runs showed excellent agreement with experimental results obtained at the Rome Laboratory Photonics Center.

In the absence of noise sources in our model, we focused on measuring receiver *noise margins* as a function of other parameters in the system. Denote the output of the I&D at time k by y_k. Denote the *correct* information bit at time k by b_k. Let $a = \min_k\{y_k, \text{given that } b_k = 1\}$, and $b = \max_k\{y_k, \text{given that } b_k = 0\}$. If $a < b$ then error-free detection is not guaranteed by any threshold setting, and a non-zero bit error rate

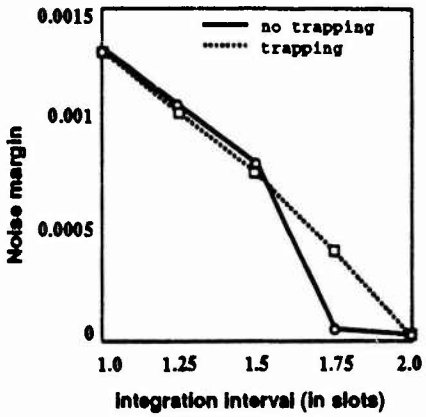

Figure 16: Noise margin as a function of integration interval (in slots). We observed 500 frames for each point. The noise margin goes to 0 as the integration interval approaches the contrast ratio, 2.0.

(BER) results, even in the absence of noise. On the other hand, if $a > b$ then error-free detection is possible by setting $b < \theta < a$. Clearly, if noise is present, the larger the difference $d = a - b$, the more immune the system is to receiver errors. We call d/I the noise margin at the receiver, where I is the I&D interval in slots.

Recall that the contrast ratio of the AND device was estimated to be approximately equal to 2.0. Also recall that our analysis showed that error-free detection is not guaranteed for integration intervals longer (in slots) than the contrast ratio. We demonstrated the effects of I&D interval length on the noise margin, by running a simulation of 160,000 samples (500 frames) for each I&D interval, ranging from 1 to 2 slots, and measuring each time the receiver noise margin. The results, as illustrated in Fig. 16, validate our analysis, and show that the noise margin goes to 0 as the integration interval (in slots) approaches the contrast ratio, 2.0. As predicted, for integration intervals longer than 2 slots, the noise margin was zero, and detection errors were unavoidable. For example, for an integration interval of 2.5 slots, we estimated a BER of 0.243, based on 500 observed frames.

Timing and synchronization are important issues in digital communications, especially in a multiple-access environment. For the system under consideration, correct timing of the received clock signal is of great practical interest, since under realistic conditions even

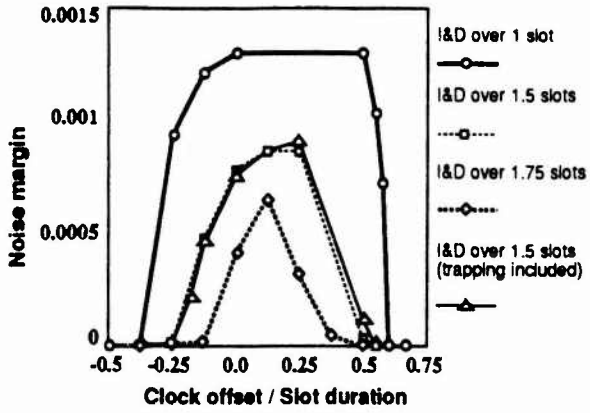

Figure 17: Noise margin as a function of clock offset (in slots). We observed 500 frames for each point. The effect of the clock offset is most dramatic for the longer integration intervals.

small inaccuracies in the length of the optical fiber can lead to significant delays at the receiver. To study the effects of unwanted delays of the clock signal on the performance of the receiver, we measured the noise margin for a variety of clock offsets. We used 500 frames per simulation run. The results are illustrated in Fig. 17. Clearly, the effect of the clock offset is most dramatic for the longer integration interval cases. Due to the effects discussed in the previous paragraph, as the integration interval becomes longer the margin for timing errors becomes smaller. Note that a clock offset of 0.75 slots in the figure corresponds to a time differential of 0.75×5 ps ≈ 4 ps. This differential could result from an error of less than 1 mm in the length of the optical fiber. Thus, the data presented in this section can be very useful when designing a practical system.

6 Conclusions

We have presented a model of the OTDMA architecture that relates parameters at the device level such as carrier mobility, physical geometry, charge trapping, and carrier-concentration to system-level performance measures such as bit error rate and noise margin. The model is used to in Monte Carlo simulations of the OTDMA network to determine bit error rates, and noise margins as a function of I&D filter bandwidth and

timing error.

In addition, have presented a simulation methodology that uses ANN to build and efficiently implement block models of nonlinear devices and subsystems within larger communication system models. We illustrated how ANN can be used in conjunction with simple subsystem block models in order to improve the simulation accuracy of such block models.

The usefulness of the ANN methodology was illustrated by showing run time savings ranging from a factor of two to a factor of three in the simulation of an OTDMA architecture that involves a two input optoelectronic AND device.

An interesting conclusion from this work is that to reduce the I&D filter bandwidth in the receiver to the bandwidth of an individual electronic processor, the contrast ratio of the photoconductive AND device must be much larger than 2:1 for a large network. Also, for the device studied in this report, at Gb/s speeds, device geometry has a much stronger influence on the contrast ratio than other device parameters.

References

[1] Paul R. Prucnal, Mario A. Santoro, and Sanjay K. Sehgal. Ultrafast All-Optical Synchronous Multiple Access Fiber Networks. *IEEE J. Select. Areas Commun.*, SAC-4(9):1484–1493, 1986.

[2] P. R. Prucnal, M. F. Krol, and J. L. Stacy. Demonstration of a Rapidly Tunable Optical Time-Division Multiple-Access Coder. *IEEE Photonics Technol. Letters*, 3(2):170–172, Feb. 1990.

[3] R. K. Boncek, P. R. Prucnal, M. F. Krol, S. T. Johns, and J. L. Stacy. 5 Gb/s Operation of a 50 Channel Optical Time-Division Multiple-Access Network. To appear in *Optical Eng.*

[4] E. Desurvire, B. Tell, I. P. Kaminow, K. F. Brown-Goebeler, C. A. Burrus, B. I. Miller, and U. Koren. 1 GHz GaInAs: Fe Photoconductive Optical AND Gate with

~ 100 fJ Switching Energy for Time-Division Access Fibre Networks. *Electronics Letters*, 25(2):105–107, 19 Jan. 1989.

[5] E. Desurvire, B. Tell, I. P. Kaminow, G. J. Qua, K. F. Brown-Goebeler, C. A. Burrus, B. I. Miller, and U. Koren. High Contrast GaInAs: Fe Photoconductive Optical AND Gate for Time-Division Demultiplexing. *Electronics Letters*, 24(7):396–397, 31 Mar. 1988.

[6] M. C. Jeruchim, P. Balaban, and K. S. Shanmugan. *Simulation of Communication Systems.* Plenum Press, 1992.

[7] M. Schetzen. *The Volterra and Wiener Theories of Nonlinear Systems.* John Wiley & Sons, 1980.

[8] W. J. Rugh. *Nonlinear System Theory.* The Johns Hopkins University Press, 1981.

[9] M. F. Tenorio and W. Lee. Self-Organizing Network for Optimum Supervised Learning. *IEEE Trans. Neural Networks*, 1(1):100–110, Mar. 1990.

[10] K. S. Narendra and K. Parthasarathy. Identification and Control of Dynamical Systems Using Neural Networks. *IEEE Trans. Neural Networks*, 1(1):4–26, Mar. 1990.

[11] W. T. Miller, III, R. S. Sutton, and P. J. Werbos. *Neural Networks for Control.* MIT Press, 1990.

[12] Philippe A. Perrier and Paul R. Prucnal. Self-Clocked Optical Control of a Self-Routed Photonic Switch. *IEEE J. Lightwave Technol.*, 7(6):983–989, 1989.

[13] D. Quinney. *An Introduction to the Numerical Solution of Differential Equations.* Research Studies Press Ltd, Lechtworth, England, 1985.

[14] P. Henrici. *Elements of Numerical Analysis.* John Wiley, New York, 1964.

[15] R. E. Crochiere and L. R. Rabiner. *Multirate Digital Signal Processing.* Prentice Hall, 1983.

[16] M. Pent *et al.* Multirate Sampling Techniques for Simulation of Communication Systems. In *Proc. IASTED Int. Sympos. on Modeling, Identification and Control*, Grindewald, Switzerland, Feb. 1987.

[17] D. Gabor, W. P. L. Wilby, and R. Woodcock. A Universal Nonlinear Filter, Predictor and Simulator which Optimizes itself by a Learning Process. *Proc. Inst. Electrical Eng.*, 108B:422–438, 1961.

[18] R. J. Roy and J. Sherman. A Learning Technique for Volterra Series Representation. *IEEE Trans. Automat. Contr.*, 12(6):761–764, Dec. 1967.

[19] A. J. Maren, C. T. Harston, and R. M. Pap. *Handbook of Neural Computing Applications.* Academic Press, 1990.

[20] R. P. Lippmann. An Introduction to Computing with Neural Nets. *IEEE ASSP Magazine*, pages 4–22, April 1987.

[21] K. Hornik, M. Stinchcombe, and H. White. Multilayer Feedforward Networks Are Universal Approximators. *Neural Networks*, 2:359–366, 1989.

[22] J. Hertz, A. Krogh, and R. G. Palmer. *Introduction to the Theory of Neural Computation.* Addison-Wesley, 1991.

[23] T. D. Sanger. A Tree-Structured Adaptive Network for Function Approximation in High-Dimensional Spaces. *IEEE Trans. Neural Networks*, 2(2), Mar. 1991.

[24] D. F. Specht. A General Regression Neural Network. *IEEE Trans. Neural Networks*, 2(6):568–576, Nov. 1991.

[25] S. Qin, H. Su, and T. J. McAvoy. Comparison of Four Neural Net Learning Methods for Dynamic System Identification. *IEEE Trans. Neural Networks*, 3(1):122–130, Jan. 1992.

[26] J. Vlach and K. Singhal. *Computer Methods for Circuit Analysis and Design.* New York: Van Nostrand Reinhold, 1983.

[27] C. H. Lee. Picosecond Optics and Microwave Technol. *IEEE Trans. Microwave Theory and Techniques*, 38(5):596–607, 1990.

[28] C. H. Lee, P. S. Mak, and A. P. Defonzo. Optical Control of Millimeter-Wave Propagation in Dielectric Waveguides. *IEEE J. Quantum Electronics*, QE-16(3), 1980.

[29] C. H. Lee and V. K. Mathur. Picosecond PHotoconductivity and its Applications. *IEEE J. Quantum Electronics*, QE-17(10):2098–2112, 1981.

[30] A. E. Iverson and D. L. Smith. Mathematical Modeling of Photoconductor Transient Response. *IEEE Electron Devices*, ED-34:2098–2107, Oct. 1987.

[31] A. E. Iverson. Mathematical Modeling of Photoconductive Power Switches. *Transactions Soc. for Computer Simul.*, 5(3):175–191, 1988.

[32] S.N. Chamoun, R. Joshi, E.N. Arnold, R.O. Grondin, K.E. Meyer, M. Pessot, and G.A. Mourou. Theoretical and Experimental Investigations of Subpicosecond Photoconductivity. *J. Appl. Physics*, 66(1):236–246, Jul. 1989.

[33] W. T. White III, C. G. Dease, M. D. Pocha, and G. H. Khanaka. Modeling GaAs High-Voltage, Subnanosecond Photoconductive Switches in One Spatial Dimension. *IEEE Trans. Electron Devices*, 37(12), 1990.

[34] R. P. Joshi and R. O. Grondin. A Self Consistent Monte-Carlo Method for the Transient Response of Laser Excited Photoconductors. *Solid-State Electronics*, 32(12):1813–1817, 1989.

[35] Y. Lu, R. P. Joshi, S. M. El-Ghazaly, and R. O. Grondin. Time-Domain Finite Difference and EMC Study of Hot Carrier Transport in GaAs on the Picosecond Scale. *Solid State Electronics*, 32(12):1297–1301, 1989.

MISSION

OF

ROME LABORATORY

Rome Laboratory plans and executes an interdisciplinary program in research, development, test, and technology transition in support of Air Force Command, Control, Communications and Intelligence (C3I) activities for all Air Force platforms. It also executes selected acquisition programs in several areas of expertise. Technical and engineering support within areas of competence is provided to ESC Program Offices (POs) and other ESC elements to perform effective acquisition of C3I systems. In addition, Rome Laboratory's technology supports other AFMC Product Divisions, the Air Force user community, and other DOD and non-DOD agencies. Rome Laboratory maintains technical competence and research programs in areas including, but not limited to, communications, command and control, battle management, intelligence information processing, computational sciences and software producibility, wide area surveillance/sensors, signal processing, solid state sciences, photonics, electromagnetic technology, superconductivity, and electronic reliability/maintainability and testability.